

# Materials Science at the Swiss Light Source

Bruce D. Patterson, Rafael Abela, and J. Friso van der Veen\*

**Abstract:** This article describes a state-of-the-art hard X-ray beamline for materials science at a third-generation synchrotron light source presently being commissioned in Switzerland, together with two typical pieces of experimental work for which the beamline is being optimized. After a discussion of the motivation, photon source, optics and experimental stations of the beamline, we present the results of some X-ray scattering studies of order–disorder phenomena that were recently performed at other synchrotron radiation sources (HASYLAB, Hamburg, and ESRF, Grenoble). The phenomena to be discussed are spontaneous ordering in epitaxial  $\text{Al}_x\text{Ga}_{1-x}\text{As}$  films and confinement-induced ordering of colloidal solutions.

**Keywords:** Confined fluids · Materials science beamline · Spontaneous ordering in epitaxial layers · Synchrotron radiation

## 1. Introduction

Since the discovery of X-ray radiation by Wilhelm Conrad Röntgen one hundred years ago, X-ray sources have become thirteen orders of magnitude brighter. At the basis of this leap forward are electron storage rings, which since the sixties came into use as sources of electromagnetic radiation. The very first synchrotrons, generally dedicated to particle physics, delivered radiation for use in a parasitic mode. The ones of the second generation were fully dedicated to users of synchrotron radiation. The radiation was produced primarily by bending magnets along the circumference of the ring, but wigglers and undulators became increasingly important as radiation sources. The third-generation synchrotrons are high-brilliance machines optimized for the performance of undulators.

Over the years, the community of users has grown explosively. Worldwide, ca. 40 synchrotron radiation sources now provide more than  $10^6$  user hours per year to a broad community of scientists in biology, physics and chemistry. A sizea-

ble fraction (in Europe more than 50%) of this beamtime is used for structural research.

A modern source is ideally expected to deliver a high brilliance over a wide photon energy range well into the hard X-ray part of the spectrum (*e.g.* 20 keV or even higher). High-energy storage rings such as ESRF (Grenoble), Spring-8 (Himeji), and APS (Argonne) are in that category. However, medium-energy storage rings with very low emittance are now being constructed, in which minigap undulators will produce harmonics up to a photon energy of *e.g.* 15 keV at an intensity comparable with that of the higher-energy sources. The Swiss Light Source will be the first medium-energy source of this type. It will serve the needs of a growing community of structural biologists and materials scientists that use synchrotron radiation for their crystallographic research.

In this article we describe the materials science beamline at SLS, along with some experiments for which this beamline is particularly well suited.

## 2. The Materials Science Beamline at the Swiss Light Source

In the first phase of beamline construction at the Swiss Light Source (first light on samples in summer, 2001), the following beamlines are planned: (a) ma-

terials science (MS), (b) protein crystallography (PX), (c) surfaces and interfaces spectroscopy (SIS), and (d) surfaces and interfaces microscopy (SIM). An overview of the characteristics of these beamlines is given in the Table. The MS beamline will produce a high flux of hard X-rays and sequentially serve three experimental stations: microtomography, powder diffraction, and *in-situ* surface diffraction.

### 2.1. Motivation

The microtomography instrument is capable of imaging samples in three dimensions at micrometer resolution. Of particular interest are studies of porous, composite and fiber-reinforced construction materials, biocompatible materials, and medical biopsy samples of bone and soft tissue. There is also interest in imaging microelectronic components, sand, rock and fossil samples, and archaeological artifacts, and in studying samples *in-situ* under stress.

The powder diffraction instrument is equipped with both a high-resolution, multi-crystal analyzer detector and with a fast-readout, position-sensitive microstrip detector. The former is for highest-resolution structure analysis, and the latter detector will allow real-time investigations of phase changes and solid-state reactions. Plans exist to use the instrument in both modes for studies of residual stress in plasma-sprayed coatings, dis-

\*Correspondence: Prof. Dr. J.F. van der Veen  
Swiss Light Source,  
Paul Scherrer Institut  
CH-5232 Villigen  
Tel.: +41 56 310 5118  
Fax: +41 56 310 3151  
E-Mail: friso.vanderveen@psi.ch

Table. The first beamlines to be realized at the Swiss Light Source.

	Photon source	Energy range [keV]	Experimental techniques
MS	Minigap wiggler	5–40	Microtomography Powder diffraction Surface diffraction
PX	In-vacuum undulator	5–18	Microfocus diffraction Large-unit cell diffraction
SIM	Permanent magnet undulator	0.2–2	Photoelectron microscopy Display analyzer
SIS	Electromagnet undulator	0.01–0.8	High-resolution photoemission Angle-resolved photoemission

location dynamics in deformed nanocrystalline metals, structural reconfigurations in nanocrystallite superlattices, and hydrogen loading in intermetallic storage materials. Also of great interest are 'smart materials' [1], which, due to the near coexistence of two crystalline phases, undergo structural transitions in response to subtle environmental changes. Examples are: electrostrictive titanates and niobates, relaxor ferroelectric perovskites, shape-memory alloys, nanostructured ferromagnets, and magnetorheological liquid crystals; they find applications in novel sensors and actuators.

Situated at the end of the beamline, a large surface diffractometer accepts user-specific process chambers for *in-situ* studies of thin-film and surface processes. Surface-sensitivity is provided by a combination of glancing incidence and the observation of extended, surface-specific distributions of scattered intensity, so-called 'crystal truncation rods' (CTRs) [2]. Phenomena to be studied with the *in-situ* surface-diffraction instrument are: epitaxial growth, island formation, surface melting and ordering phenomena at solid surfaces and at solid-liquid interfaces. The structural response of thin-film materials to electromagnetic fields, electrochemical environment and plasma interactions can also be studied, with surface sensitivity. It is foreseen that the sample preparation equipment can also be used for photoemission experiments on the SIS and SIM beamlines. An epitaxial growth method which deserves special mention is pulsed laser deposition. Being an athermal technique with highly-excited precursors, it is capable of producing stoichiometric films containing many atomic species, without the need of dangerous reactants. The addition of a coordinated pulsed gas source results in 'pulsed reactive crossed-beam laser ablation' [3], expanding the range

of crystals which can be grown to, e.g. large-bandgap semiconducting nitrides and super-hard carbonitrides. A particularly attractive feature of pulsed laser deposition for *in-situ* diffraction studies involves the time-structure of the deposition process; by synchronizing the laser pulses and the data acquisition, it is possible to follow the post-pulse migration of the deposited species to their equilibrium sites.

## 2.2. Photon Source and X-Ray Optics

The principal components of the SLS machine are: a thermionic electron gun, a 100 MeV LINAC injector, a 2.4 GeV booster synchrotron and the 2.4 GeV storage ring. Semi-continuous 'top-up' injection into the storage ring will maintain a constant heat load on the beamline optical components. The ring has a circumference of 288 m, and it has an approximate twelve-fold symmetry, each twelfth having a straight section of one of three lengths, 4, 7 or 11 m, for insertion devices. Between adjacent straight sections, the central dipole of which can produce two independent synchrotron light beams with a critical energy of 4 keV. The maximum current in the ring is 400 mA, and several fill modes are available for time-dependent experiments. The horizontal and vertical rms widths of the electron beam at the MS wiggler are 76 and 8  $\mu\text{m}$ , respectively.

The light source for the MS beamline is a hybrid minigap wiggler, which produces a continuous spectrum of photons with a critical energy (dividing the spectrum into two parts with equal integrated intensities)  $E_c = 7.9$  keV. A combination of NdFeB permanent magnets and Permenur pole pieces produces a maximum field of 1.97 T, at a wiggler period of 61 mm and a magnetic gap of 7.5 mm. The

wiggler is 2 m long and radiates a total of 8.4 kW. At 10 keV, the wiggler emits approximately  $2 \times 10^{15}$  photons/s/0.1% bandwidth into an approximately Gaussian profile, with horizontal and vertical FWHM of 2.7 and 0.25 mrad, respectively. A special vacuum chamber, with a vertical vacuum gap of 5.5 mm, carries the electron beam through the wiggler. The relatively high residual gas pressure in this narrow chamber represents a strong source of high-energy Bremsstrahlung radiation. A front end safety system consists of a beam-defining aperture, followed by a beam shutter, a carbon filter, beam position monitors, primary slits and a double Be window. The radiation power leaving the front end is 2.1 kW, the spectrum being cut off by Be absorption below 4 keV.

The beamline optics are shown schematically in Fig. 1. The first mirror provides vertical collimation and removes short-wavelength harmonics of the monochromator. The mirror consists of a 1 m long, Rh-coated Si blank, which can be tilted and bent ( $R_{min} = 5$  km) as required for the desired photon energy. The surface of the mirror is polished to a rms roughness of less than 0.2 nm and to a rms residual slope error less than 1  $\mu\text{rad}$ . The mirror is cooled (maximum absorbed heat load of 1 kW) by water-cooled blades immersed in Ga-In-Sn eutectic in grooves in the mirror surface.

The double crystal monochromator consists of two Si(111) crystals which can be precisely positioned and oriented in the X-ray beam. Two successive Bragg reflections, with an inherent energy resolution of 0.014%, direct photons of the desired energy parallel to the incoming beam direction, but offset downward by 15 mm. This 'fixed exit' operation is achieved by placing both crystals on a common rotation stage, with the diffracting surface of crystal 1 on the rotation axis, and translating crystal 2 along two perpendicular directions within the scattering plane. The large heat load absorbed by the first crystal (up to 1 kW) causes it to deform, and a water-cooled, mechanical bending apparatus, developed at HASYLAB, Hamburg [4], dynamically corrects this curvature. The second crystal provides horizontal focusing; it is a ribbed crystal, cylindrically bent to a variable radius ( $R_{min} = 1$  m) in a flexure-hinge fixture developed at the ESRF, Grenoble [5].

The second mirror is similar to the first. A variable curvature will permit vertical focusing at the experimental station in use. Since this focusing introduces

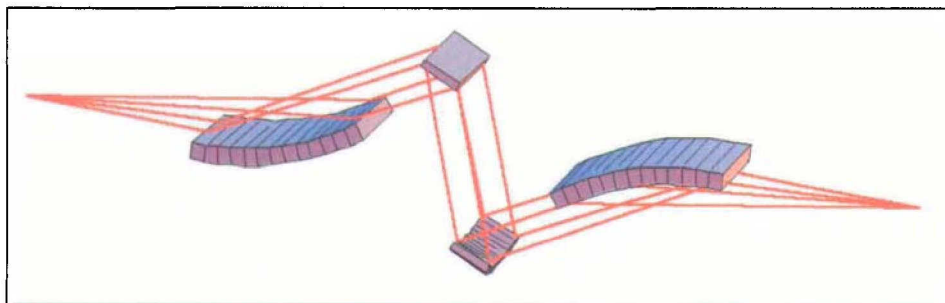


Fig. 1. A schematic view of the optics of the MS beamline, showing the vertically-collimating mirror, the flat and horizontally-focusing crystals and the vertically-focusing mirror.

a divergence which is undesirable in high-resolution powder diffraction, the user may choose to either set the radius of curvature of the second mirror to infinity or to remove it from the beam altogether, the latter option resulting in an inclined beam.

The MS beamline produces a monochromatic spectral flux density at 10 keV of approximately  $10^{13}$  photons/s/0.1% bandwidth, which can be focused to a 1 mm<sup>2</sup> spot at the experimental stations. Polychromatic radiation is also available by driving the monochromator crystals out of the beam. Local beam shutters allow access to the experiments while the optics are kept warm, and a control system based on standard software is used to adjust the optical elements and to run the experiments.

### 2.3. Experimental Stations

A user consortium is responsible for designing, constructing and installing a state-of-the-art microtomography instrument [6] with high spatial resolution and with both absorption- and phase-contrast measurement capabilities. The instrument takes monochromatic beam and incorporates a precision sample translation/rotation stage and an X-ray camera consisting of a scintillator and a CCD. A key component is a two-dimensional magnifier stage after the sample, which relies on diffraction by asymmetrically-cut silicon crystals.

The powder diffractometer is based on three coaxial, high-precision rotary tables. The inner table, with a reproducibility of better than 2 arc seconds, alternatively carries a capillary spinner, a flat-plate holder or an Eulerian cradle. In addition, it mates to a separately-supported He-flow cryostat and other, user-specific, sample environment equipment. The middle table, with a reproducibility of 5 arc seconds, holds a 15000 element Si microstrip detector, developed at the Paul Scherrer Institute. The detector can be precisely positioned in  $2\theta$ , allowing easy

calibration and great flexibility in its operating modes (e.g. simultaneous high-low resolution measurements in conjunction with the analyzer-detector, complementary operation for improved statistics at high  $2\theta$ -values, etc.). Readout of all 15000 elements requires 10 ms. The outer table of the diffractometer has a reproducibility of 2 arc seconds and carries the high-resolution 5-fold silicon crystal analyzer / scintillation detector system. If sufficient interest arises, it will be possible to mount samples on the diffractometer with a robotic changing device and to control the measurements *via* the Internet.

The *in-situ* surface diffractometer is of the '2+3' design [7] (see Fig. 2). With this geometry, removable 'baby' chambers weighing up to 25 kg can be mounted with the sample surface vertical (for CTR measurements) or up to 100 kg with the sample horizontal (for precisely-defined incidence angles). In addition, it is possible, with the sample surface vertical, to independently support a heavy *in-situ* process chamber (<600 kg) on a rotation table of the diffractometer, the sample being positioned *via* a flexible bellows and a UHV rotational feedthrough. The scintillation detector has rotatable slits, for proper intensity normalization, and an analyzer crystal, to reduce background

and avoid parallax. Although PSI is constructing several 'standard' process chambers, it is the responsibility of the individual research groups to provide and maintain their own chamber, specific to their process and measurement.

### 3. Spontaneous Ordering in Epitaxial Al<sub>x</sub>Ga<sub>1-x</sub>As

The ternary III-V semiconductor Al<sub>x</sub>Ga<sub>1-x</sub>As is generally grown as an epitaxial layer, normally on a (001) oriented GaAs substrate. Due to the closely similar covalent radii of Al and Ga, layers in the entire composition range  $0 < x < 1$  and with a thickness up to several hundreds of nm can be grown with negligible densities of misfit dislocations. Heterostructures of Al<sub>x</sub>Ga<sub>1-x</sub>As/GaAs are routinely used in fundamental quantum-well physics as well as in devices such as high-mobility transistors and semiconductor laser diodes.

The small lattice strain in Al<sub>x</sub>Ga<sub>1-x</sub>As is generally believed to preclude phase separation and long-range order, implying that Al and Ga occupy random positions on the group-III sublattice of the zincblende structure. In spite of this, the first evidence of long-range order in *any* III-V ternary alloy was found in 1985 by Kuan *et al.* [8], in Al<sub>x</sub>Ga<sub>1-x</sub>As grown on (110) GaAs substrates. Using electron diffraction, they observed superlattice diffraction peaks corresponding to an ordering of Al and Ga in the CuAu I type structure. Since that time, no further experimental observation of spontaneous ordering in Al<sub>x</sub>Ga<sub>1-x</sub>As has been published, although ordering has been found in other III-V systems [9]. Several theoretical investigations of the stability of CuAu I ordered Al<sub>x</sub>Ga<sub>1-x</sub>As have been made [9], but Al<sub>x</sub>Ga<sub>1-x</sub>As remains 'the least understood case'. For this reason,

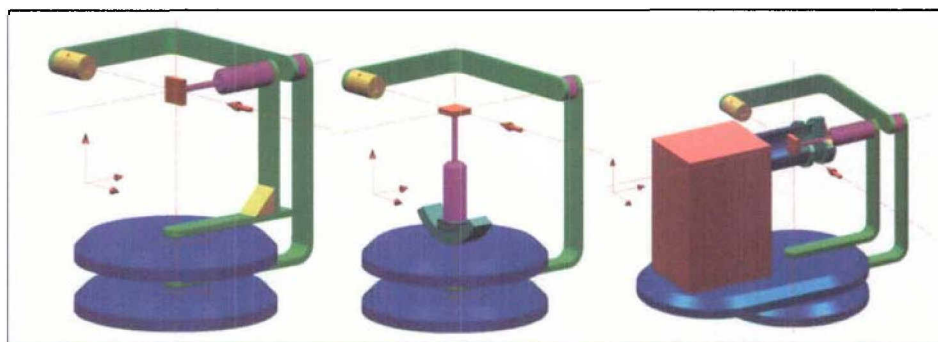


Fig. 2. The measurement geometries possible with the *in-situ* surface diffractometer: with a vertical sample in a baby chamber (left), with a horizontal sample in a portable chamber (center), and with a vertical sample in a heavy *in-situ* process chamber (right).

and in view of the much higher resolution available with X-ray diffraction, we undertook a search with synchrotron radiation diffraction for spontaneously ordered  $\text{Al}_x\text{Ga}_{1-x}\text{As}$  [10].

### 3.1. The CuAu I Ordered Structure

Our samples were grown with organo-metallic vapor phase epitaxy (OMVPE) on a (110) GaAs substrate, at a pressure of 0.08 bar. A 170 nm thick GaAs buffer layer was first grown, followed by the  $\text{Al}_x\text{Ga}_{1-x}\text{As}$  layer. The nominal conditions for the  $\text{Al}_x\text{Ga}_{1-x}\text{As}$  growth implied a composition of  $x = 0.75$ , a growth rate of 2.5  $\mu\text{m/h}$  and a layer thickness of 500 nm. The sample was terminated with an 80 nm cap layer of GaAs. The sample temperature during growth was varied between 620 and 780  $^\circ\text{C}$ . Most of the diffraction measurements were performed on beamline BM1A of the European Synchrotron Radiation Facility in Grenoble, France. The wavelength was selected with a Si(111) double crystal monochromator, and Rh-coated mirrors situated before and after the monochromator removed any harmonics shorter in wavelength than 0.55  $\text{\AA}$ . The two-dimensional scattered intensity in reciprocal space was mapped with  $\omega$ - and  $\theta$ -2 $\theta$  scans. Transmission electron microscopy (TEM) and diffraction were also performed on the 700  $^\circ\text{C}$  sample.

To establish the presence of superstructure ordering, a number of 'zincblende-allowed' ( $h, k, l$  all even or  $h, k, l$  all odd), 'CuAu I-allowed' ( $h + k$  even and  $k + l$  odd) and 'forbidden' (otherwise) reflections were recorded for the 700  $^\circ\text{C}$  sample (see Fig. 3a). Strong zincblende-allowed reflections are observed from the substrate and the  $\text{Al}_x\text{Ga}_{1-x}\text{As}$  layer, split by the small elastic distortion of the layer. In addition, one clearly sees much weaker CuAu I reflections arising from ordered  $\text{Al}_x\text{Ga}_{1-x}\text{As}$ . The integrated intensity ratio between the superlattice 110 reflection and the zincblende-allowed 220  $\text{Al}_x\text{Ga}_{1-x}\text{As}$  layer reflection is  $2.9 \times 10^{-4}$ . In no case was a forbidden reflection observed, verifying the single-domain character of the structure. The perfectly ordered CuAu I crystal structure of  $\text{Al}_{0.5}\text{Ga}_{0.5}\text{As}$  is shown in Fig. 3b.

The weak intensity of the superstructure reflections can be attributed to either a small volume fraction of the ordered phase, or to an order parameter less than unity – we discriminate between these possibilities as follows. Due to the lattice mismatch  $\Delta a/a$  between the  $\text{Al}_x\text{Ga}_{1-x}\text{As}$  layer and the (110) GaAs substrate, the layer will experience a tetragonal distor-

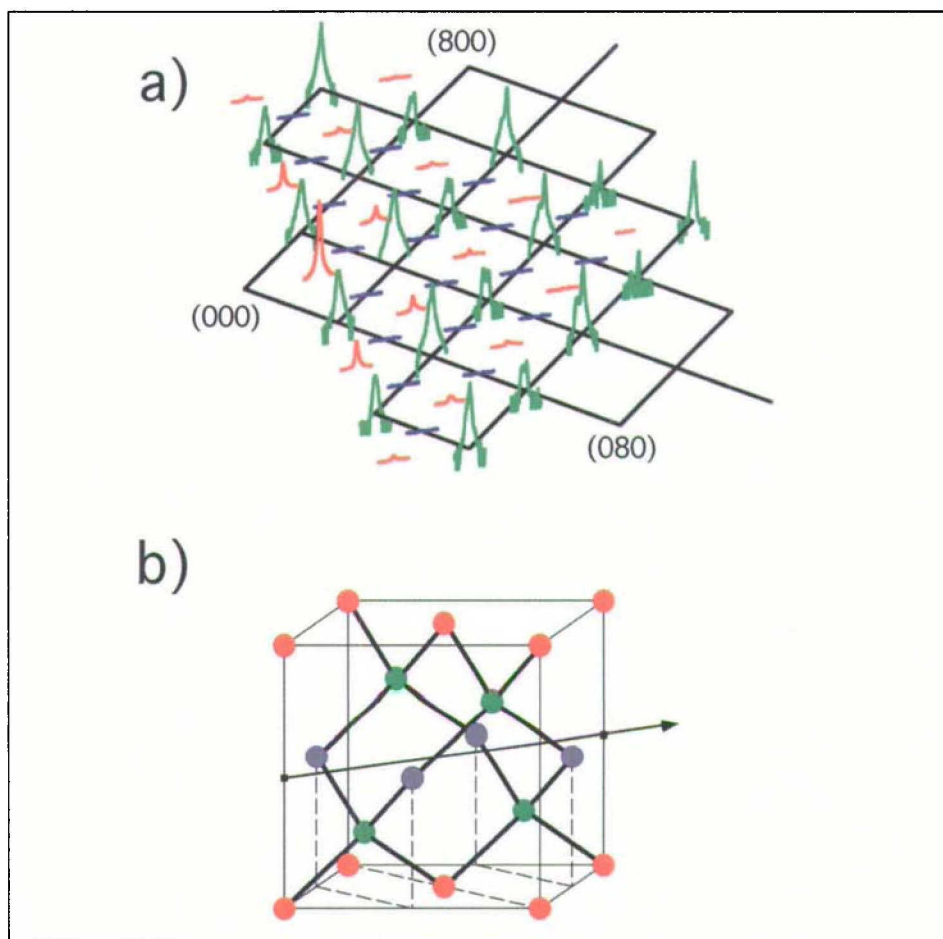


Fig. 3. (a) A summary of measured Bragg reflections of type  $(hk0)$ , taken at a photon wavelength of 0.7138  $\text{\AA}$ . The 'zincblende-allowed' reflections ( $h, k, l$  all even or  $h, k, l$  all odd) from the GaAs substrate and disordered  $\text{Al}_x\text{Ga}_{1-x}\text{As}$ , are plotted on a logarithmic scale, and the 'CuAu I-allowed' reflections ( $h + k$  even or  $h + k$  odd) from ordered  $\text{Al}_x\text{Ga}_{1-x}\text{As}$ , as well as the remaining 'forbidden' reflections, are plotted on the same linear scale. (b) The ideal CuAu I crystal structure of ordered  $\text{Al}_{0.5}\text{Ga}_{0.5}\text{As}$ . White, gray and black circles represent Ga, Al and As ions, respectively, and the arrow indicates the (110) growth direction. Measurement performed at beamline BM1A of ESRF, Grenoble.

tion. From simple elasticity theory, the relation between  $\Delta a/a$  and  $\Delta d/d$ , the relative change in the (110) planar spacing, is determined to be:

$$\frac{\Delta d}{d} = \frac{2(C_{11} + 2C_{12})}{(C_{11} + C_{12} + 2C_{44})} \frac{\Delta a}{a} \approx 1.60 \frac{\Delta a}{a} \quad (1)$$

where the  $C_{ij}$  are the elastic moduli.

It is assumed here, and verified for our sample by observation of asymmetric Bragg reflections, that the strain is purely elastic, *i.e.* without plastic relaxation. Rocking curves for the CuAu I-allowed 330 and zincblende-allowed 440 reflections were taken on the 700  $^\circ\text{C}$  sample at  $\lambda = 1.1325 \text{\AA}$ , *i.e.* sufficiently long that the higher-order 660 reflection at  $\lambda/2$  was simultaneously passed by the beamline mirrors, providing a reference substrate reflection for the 330 peak. From the observed substrate-layer splittings  $\Delta\theta$ , we compute the changes in the (110) layer spacings  $\Delta d/d = \Delta\theta/\tan\theta$  for the 330 ordered and the 440 disordered reflections.

Further, using the measured  $x$ -dependence [11] of the  $\text{Al}_x\text{Ga}_{1-x}\text{As}$  elastic moduli, we are able to determine that the aluminum fractions pertinent to the ordered and disordered reflections are in approximate agreement:  $x_{330} = 0.566(2)$ ,  $x_{440} = 0.587(9)$ . This observation of a uniform Al fraction not equal to 0.5 implies that a simple phase separation model, with a fraction of the sample in the ordered  $\text{Al}_{0.5}\text{Ga}_{0.5}\text{As}$  phase and the remainder in a disordered  $\text{Al}_x\text{Ga}_{1-x}\text{As}$  phase, is untenable.

Under the assumption of a homogeneous but imperfectly-ordered sample, the order parameter  $S = r_{\text{Al}} + r_{\text{Ga}} - 1$ , where  $r_{\text{Al}}$  and  $r_{\text{Ga}}$  are the fractions of the Al and Ga sites occupied by the correct atom, respectively [8], can be evaluated from a quantitative comparison of the CuAu I and zincblende-allowed diffraction intensities. From the observed integrated intensity ratio  $I(110)/I(220) = 2.9(1) \times 10^{-4}$ , we determine that  $S = 6.4(1)\%$ .

### 3.2. Defects in the Superstructure

A further test of the sample homogeneity can be made using cross-sectional TEM. Micrographs from the 700 °C sample, taken close to the GaAs substrate, show striations running parallel to the film-substrate interface. An autocorrelation function computed from a horizontal projection of the TEM data [10] shows both a short-range (2.5 nm) correlation, superimposed on a quasi-periodic oscillation with a 20 nm period. We attribute the former to random stacking faults, and the latter to composition striations. Stacking faults in the CuAu I ordered structure should broaden the X-ray diffraction profile in a  $\theta$ - $2\theta$ -scan, and we have measured the extent of the diffuse scattering in the 700 °C sample over a large range in  $\omega$  (see Fig. 4). An example of a possible fit to the data consists of a linear background plus three Voigt functions, corresponding to stacking-fault correlation lengths of 2.2, 26 and >80 nm. Note the agreement between the short-range correlation length seen near the substrate with TEM and the largest component of the diffraction linewidth.

How could the degree of superstructure ordering in (110)  $\text{Al}_x\text{Ga}_{1-x}\text{As}$  be improved? An important degree of freedom in the layer growth is the substrate temperature. A comparison of the (110) superstructure  $\theta$ - $2\theta$  diffraction intensity for four growth temperatures (Fig. 5) demonstrates that 700 °C is close to optimal, yielding a minimum linewidth. This finding is in good agreement with the electron diffraction results of Kuan *et al.* [8].

The presence of the additional narrow components in the  $\theta$ - $2\theta$  X-ray scan (Fig. 4) implies the existence of regions in the sample with a low density of stacking faults. We were able, by changing the TEM focusing conditions to diffraction, to observe clear superstructure electron diffraction reflections from the sample. No significant change in the diffraction pattern was seen as the electron beam

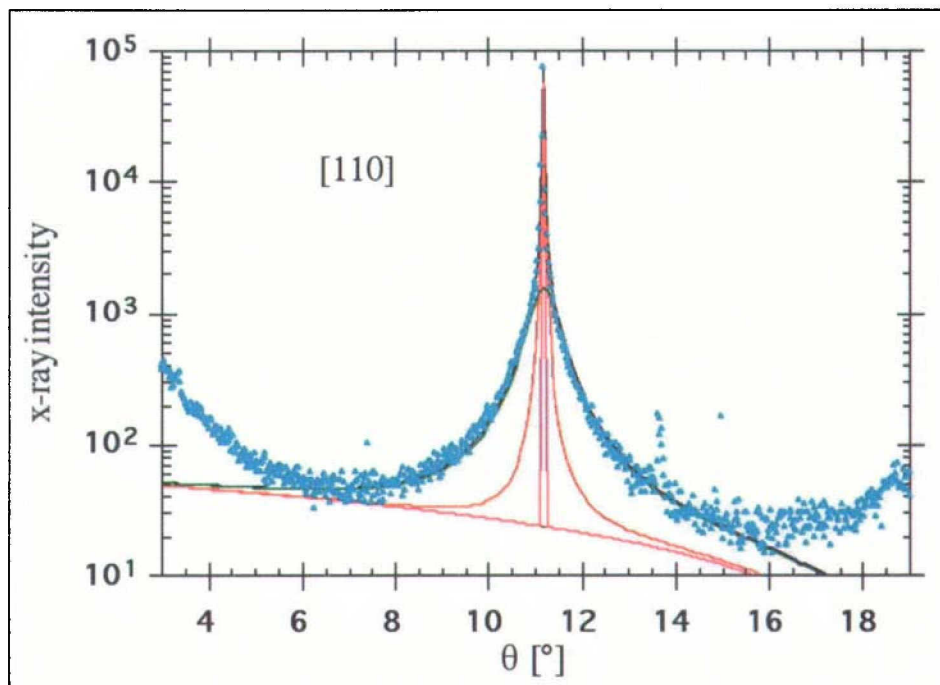


Fig. 4. Diffuse scattering around the superstructure 110 peak, measured in  $\theta$ - $2\theta$  mode at 8 keV photon energy. Measurement performed at beamline W2 of HASYLAB, Hamburg.

was scanned over a distance of 10  $\mu\text{m}$  parallel to the substrate-layer interface. On the other hand, a large change in the diffraction spots was observed as the beam was moved from the just above the GaAs substrate to the top of the  $\text{Al}_x\text{Ga}_{1-x}\text{As}$  layer. Near the substrate, the superstructure reflections showed pronounced diffuse tails along the growth direction, which gradually gave way to point-like diffraction spots just below the layer surface [10]. This observation implies a progressive improvement in the superstructure order (decrease in stacking fault den-

sity) during the growth process, which is reminiscent of the increase in ordered domain size observed in OMVPE growth of GaInP on (001) GaAs [12]. Indeed, X-ray measurements at HASYLAB on 500 nm and 1500 nm thick (110)  $\text{Al}_x\text{Ga}_{1-x}\text{As}$  layers grown with OMVPE under the same conditions show an  $I(110)/I(220)$  integrated intensity ratio for the thicker layer which is 2.9 times larger than that for the thinner one. This result provides further proof of a progressive enhancement of the ordering with increasing layer thickness.

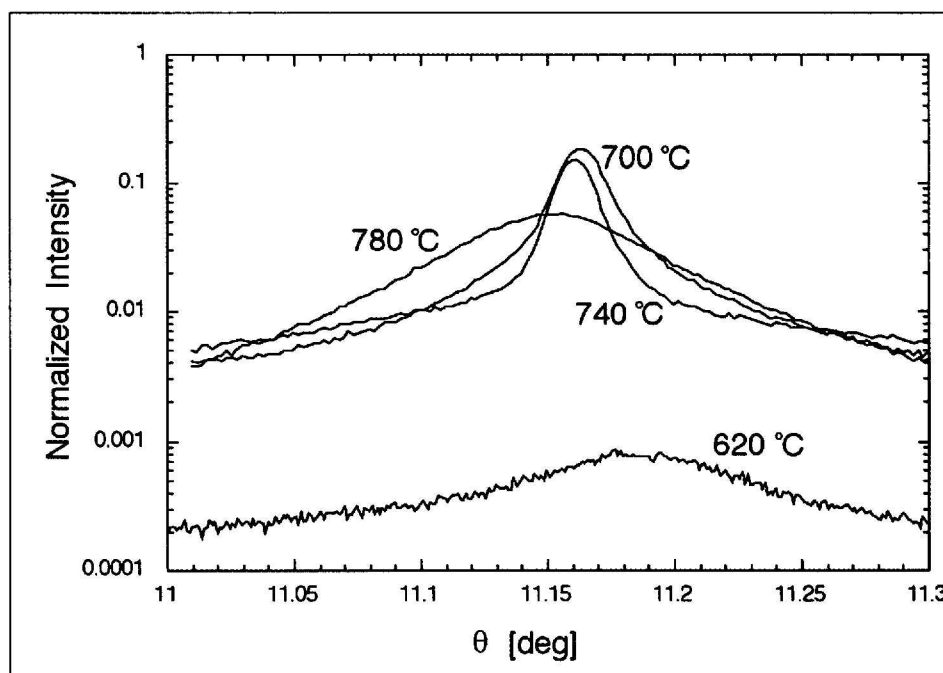


Fig. 5. Relative intensities of  $\theta$ - $2\theta$ -scans of the 110 superstructure reflection in (110)  $\text{Al}_x\text{Ga}_{1-x}\text{As}$  samples grown with OMVPE at different growth temperatures. Measurement performed at W2 of HASYLAB.

Our investigation of (110) OMVPE layers with a combination of high-resolution X-ray diffraction and electron microscopy and diffraction has yielded new information on ordering in  $\text{Al}_x\text{Ga}_{1-x}\text{As}$ , which is still a poorly understood phenomenon despite 15 years of effort since the first experimental evidence. Summarizing our results, the superstructure ordering of the epitaxial layer produced under the pertinent growth conditions is generally uniform – it is not the case that domains of highly-ordered material (with  $x = 0.5$ ) are surrounded by disordered material of a different composition. The degree of order is laterally constant, on both a microscopic ( $\mu\text{m}$ ) and a macroscopic (mm) scale. Stacking faults, oriented parallel to the substrate-layer interface, disrupt the order. These faults have the highest density close to the substrate, and the corresponding correlation length increases from approximately 2.2 nm to more than 80 nm over the 500 nm layer thickness. We have demonstrated a quantitative determination of the degree of ordering: when averaged over the layer thickness, the order parameter in our sample, grown at 700 °C, is  $S = 6.4(1)\%$ . Finally, it has been demonstrated that quasi-periodic vertical phase separation can occur simultaneously with CuAu I superstructure ordering.

Our observation that  $\text{Al}_x\text{Ga}_{1-x}\text{As}$  ordering improves with layer thickness may provide a path to the production of high-quality ordered material suitable for the investigation of transport and optical properties, and perhaps for applications. In contrast to CuPt B ordered InGaP on (001) GaAs, which is plagued by domain walls [12] between the two degenerate subvariants (111) and (1 $\bar{1}$ 1), CuAu I ordered  $\text{Al}_x\text{Ga}_{1-x}\text{As}$  on (110) GaAs is inherently single-domain.

#### 4. Ordering Phenomena in Confined Fluids

From everyday experience we know that a fluid film between two solid surfaces acts as a lubricant. Examples are fluids of alkanes, solutions of nanoparticles (*e.g.*  $\text{MoS}_2$ ) or granular systems such as clays. It is well known that the lubricating properties of the film strongly depend on its thickness, *i.e.* the degree of confinement. As the gap between the two confining surfaces decreases to a few molecule or particle diameters, the confined fluid is generally found to become stickier. This confinement effect has been attributed to a solid-like ordering of

the fluid's constituents in layers parallel to the confining surfaces. Sliding the surfaces then may induce an alternation between stick and slip [13]. During these transitions the lubricant is believed to transform repeatedly from an ordered, solid-like state to a fluid state and *vice versa*. In the solid-like state the adhesion between the sliding surfaces may be large enough to cause damage to the surfaces. From an economical viewpoint, this is highly unwanted. Besides being of technological relevance, confinement-induced ordering phenomena are interesting from a fundamental point of view.

We have developed a novel coherent X-ray scattering method for probing ordering phenomena in confined fluids. The method makes use of the waveguiding properties of the gap between the confining plates. The principle is illustrated in Fig. 6 for two parallel plates with adjustable gap width, confining a suspension of colloidal silica particles. The X-ray beam is directed into the gap along a direction nearly parallel to the

plates. Interference between the incident and reflected waves at the entrance gives rise to a standing wave pattern ('waveguide modes'), which can be made to fit exactly within the gap by adjustment of the angle of incidence or the gap width [14]. Within the plate material, the wavefield decays rapidly to zero. If the fluid were absent, the waveguide modes would propagate undisturbed through the gap. In the filled waveguide, however, the spatial variations in the electron density of the fluid give rise to scattering into other waveguide modes ('mode coupling'). The distribution of intensity over the different modes is observed as Fraunhofer diffraction patterns of the wavefield across the waveguide's exit plane. From these, the density profile is determined through a model-dependent analysis.

Here we show data for a 10 vol.% suspension of colloidal silica particles ( $\varnothing$  110 nm) in dimethylformamide, confined within a gap of 655 nm. The waveguiding experiment was performed at beamline

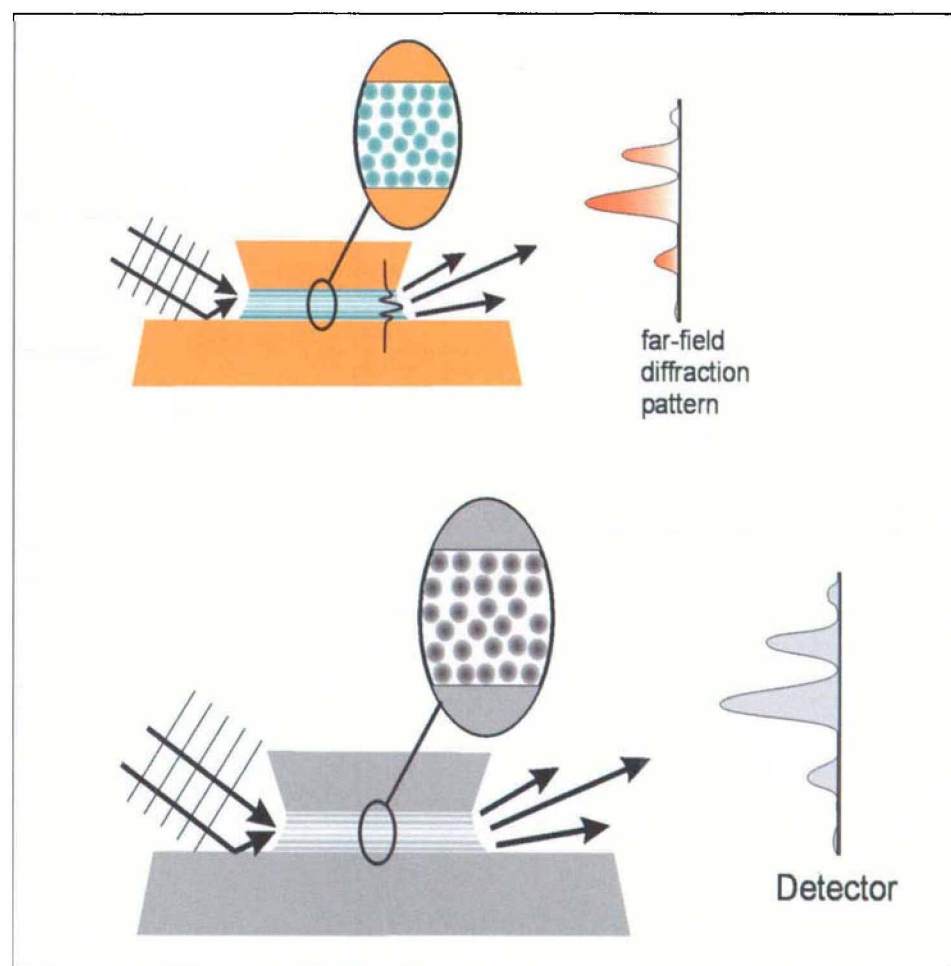


Fig. 6. Schematic of the X-ray waveguiding geometry (not to scale). The fluid within the gap has ordered into layers parallel to the plates. The incident wavefield is scattered from the layered density distribution into several waveguide modes. The distribution of intensity over these modes gives rise to a characteristic diffraction pattern in the far field, from which the density profile of the fluid across the gap can be derived.

ID10A of the ESRF, at a wavelength of 0.093 nm [15]. Fig. 7 shows a contour plot of the diffracted intensity  $I(\theta_i, \theta_e)$ , measured as a function of the incidence angle  $\theta_i$  and the exit angle  $\theta_e$ . The intense off-diagonal peaks are evidence of strong mode coupling. The same measurements for the waveguide without fluid (not shown) yield only modes along the diagonal [14]. Calculations of the intensity distributions for various models of the density profile show agreement with the data for a non-uniform filling of the gap with six close-packed layers (see the bottom panels of Fig. 7). Similar results were obtained for a gap of 310 nm, which confined two crystallized layers. In summary, the proximity of the walls induces a strong layering effect in the colloid. The ordering of the particles in a close-packed structure and the non-uniformity of the ordered regions in the plane of the

gap suggest that the confinement induces crystallization at volume densities much lower than the critical density for crystallization of bulk colloid [16].

Our method can be extended to include studies of (molecular) fluids confined within much smaller gaps. One should then make use of multi-step index waveguides and detect both guided and radiative waveguide modes [17]. Recently we have constructed a device for confinement of fluids within gaps down to a few nanometers. It has provisions for combined X-ray scattering and force measurements. Distances and forces are measured in the same way as in the surface force apparatus (SFA) developed by Israelachvili [18].

The surface-diffraction station at the MS beamline is well suited for these studies. The emittance of the minigap wiggler source is much smaller in the

vertical plane than in the horizontal plane, which is matched to the beam acceptance of the horizontally positioned confining geometry.

### Acknowledgements

BDP wishes to acknowledge the sample preparation of M. Moser and H.P. Schweizer, assistance in the synchrotron measurements of H. Auderset, K. Knudsen, R. Mathiesen, P. Pattison and O. Seeck, the TEM and electron diffraction measurements of E. Müller and enlightening discussions with U. Staub. JFvdV acknowledges the essential contributions by M.J. Zwanenburg, J.H.H. Bongaerts and G.H. Wegdam to the experiments on the confined colloids.

Received: March 30, 2001

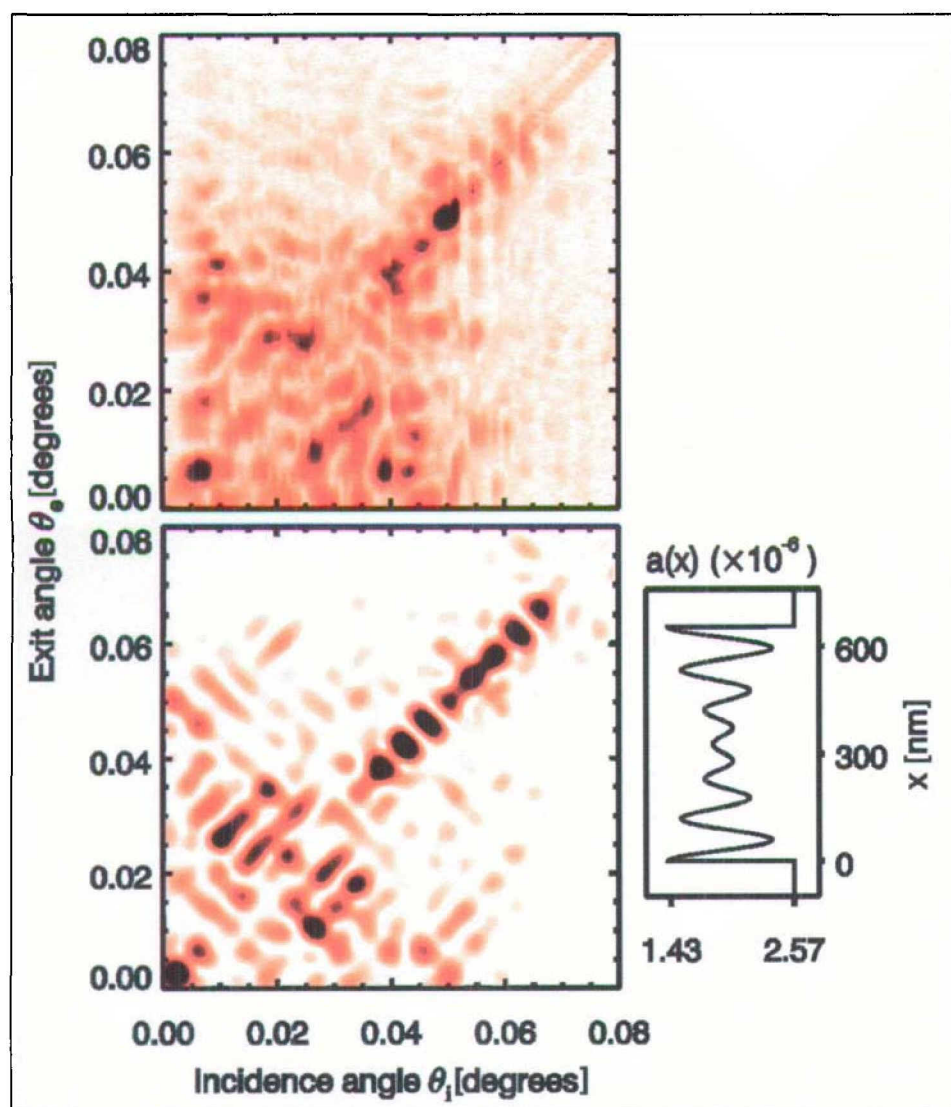


Fig. 7. Contour plot of the diffracted intensity  $I(\theta_i, \theta_e)$  for a waveguide of 4.85 mm length, having a gap of 655 nm and filled with a colloidal suspension of silica spheres ( $\varnothing$  110 nm). The angles  $\theta_i$  and  $\theta_e$  are the grazing incidence and exit angles with respect to the plane of the confining surfaces. Upper panel: measured intensity distribution. Lower panels: intensity distribution calculated for a refractive-index profile  $n(x) = 1 - a(x)$ , modeling six layers of confined fluid. Measurements performed at ID10 of ESRF, Grenoble (from [15]).

- [1] R.E. Newnham, *MRS Bulletin* **1997**, 22, 20.
- [2] E. Vlieg, I.K. Robinson, in 'Synchrotron Radiation Crystallography', Ed. P. Coppens, Academic Press, London, **1992**.
- [3] P.R. Willmott, J.R. Huber, *Rev. Mod. Phys.* **2000**, 72, 315.
- [4] H. Schulte-Schrepping, G. Materlik, J. Heuer, T. Teichmann, *Rev. Sci. Instrum.* **1995**, 66, 2217.
- [5] A.K. Freund, F. Comin, J.L. Hazemann, R. Hustache, B. Jenninger, K. Lieb, M. Pierre, *Proc. SPIE* **1998**, 144, 3448.
- [6] U. Bonse, R. Nusshardt, F. Busch, R. Pahl, Q.C. Johnson, J.H. Kinney, R.A. Saroyan, M.C. Nichols, *Rev. Sci. Instrum.* **1989**, 60, 2478.
- [7] E. Vlieg, *J. Appl. Cryst.* **1998**, 31, 198.
- [8] T.S. Kuan, T.F. Kuech, W.I. Wang, E.L. Wilkie, *Phys. Rev. Lett.* **1985**, 54, 201.
- [9] A. Zunger and S. Mahajan, in 'Handbook on Semiconductors 3', Ed. S. Mahajan, **1994**, p. 1399.
- [10] B.D. Patterson, H. Auderset, K.D. Knudsen, R.H. Mathiesen, E. Müller, P. Pattison, O. Seeck, M. Shi, U. Staub, submitted to *Phys. Rev. B*.
- [11] S. Gehrsitz, H. Sigg, N. Herres, K. Bachem, K. Köhler, F.K. Reinhart, *Phys. Rev. B* **1999**, 60, 11601.
- [12] S. Mahajan, *Inst. Phys. Conf. Ser.* **1997**, 160, 367.
- [13] B.N.J. Persson, 'Sliding Friction', Springer-Verlag, Berlin, Heidelberg, New York, **1998**.
- [14] M.J. Zwanenburg, J.H.H. Bongaerts, J.F. Peters, S.A. de Vries, D.L. Abernathy, J.F. van der Veen, *Phys. Rev. Lett.* **1999**, 82, 1696.
- [15] M.J. Zwanenburg, J.H.H. Bongaerts, J.F. Peters, D.O. Riese, J.F. van der Veen, *Phys. Rev. Lett.* **2000**, 85, 5154.
- [16] P.N. Pusey, W. van Megen, *Nature* **1986**, 320, 340.
- [17] J.H.H. Bongaerts, M.J. Zwanenburg, F. Zontone, J.F. van der Veen, *J. Appl. Phys.* **2001**, in press.
- [18] J.N. Israelachvili, P.M. McGuiggan, *J. Mater. Res.* **1990**, 5, 2223.